Analysis of foveal characteristics and their asymmetries in the normal population

Patrick Scheibe[a,b], Maria Teresa Zocher[b], Mike Francke[a,c], Franziska Georgia Rauscher[b]

[a]*Saxonian Incubator for Clinical Translation (SIKT), University Leipzig, Leipzig, Germany*
[b]*Department of Ophthalmology, Leipzig University Hospital, Leipzig, Germany*
[c]*Paul-Flechsig-Institute of Brain Research, Department of Pathophysiology of Neuroglia, University Leipzig, Leipzig, Germany*

Abstract

The advance of optical coherence tomography (OCT) enables a detailed examination of the human retina in-vivo for clinical routine and experimental eye research. Only few investigations to date captured human foveal morphology in a large subject group on the basis of a detailed analysis employing mathematical models. However, even for important foveal characteristics unified terminology and clear definitions were not implemented so far. This might be a reason, why to this day the human fovea is considered to be a mostly symmetric and round structure. Therefore, the most important finding of this work is the detailed analysis of the asymmetric structure of the human fovea. We employed five clinically highly relevant foveal characteristics, which are derived from a previously published fovea model. For each, an accurate mathematical description is given. The presented properties include (1) mean retinal thickness inside a defined radius, (2) foveal bowl area, (3) a new, exact definition of foveal radius, (4) maximum foveal slope, and (5) the maximum height of the foveal rim. Furthermore, minimum retinal thickness was derived and analyzed. 220 strictly controlled healthy Caucasian subjects of European decent with an even distribution of age and gender were imaged with an Heidelberg Spectralis OCT. Detailed analysis demonstrated the following general results: (1) significant gender difference regarding the central foveal subfield thickness (CFST) but no significant differences for the minimum central retinal thickness, (2) a strong correlation between right and left eye of the same subject, and, as essential finding, (3) strong structural differences of the fovea form in the different anatomical directions (nasal, temporal, inferior and superior). In the analysis of the foveal asymmetry, it will be demonstrated that the foveal radius is larger in nasal and temporal direction compared to inferior and superior position. Furthermore, it will be shown that the circular fovea rather has an elliptic form with the larger axis along the nasal to temporal direction. Interestingly, the foveal slope shows a divergent behavior as the temporal direction has the smallest slope angle and both, inferior and superior angles are clearly larger than the others. The findings in this work can be used for an exact quantification of changes in early stages of various retinal diseases and as a marker for initial diagnosis.

Keywords: Fovea Centralis, Fovea Pit Morphology, Mathematical Model, Optical Coherence Tomography (OCT)

1. Introduction

Optical coherence tomography (OCT) is a laser-based technique which implements laser interferometry and is able to penetrate the retina to produce sections with a very high resolution. Light from a broad-band laser source is divided into a sample and reference beam, and the reflection of both arms results in an

*Corresponding author. Tel.: +49 341 97 39483; Fax.: +49 341 97 39609; Addr.: Saxonian Incubator for Clinical Translation (SIKT) Leipzig, Philipp-Rosenthal-Straße 55, 04103 Leipzig
Email address: pscheibe@sikt.uni-leipzig.de (Patrick Scheibe)

interference image which contains information of the sample. Based on spectrometry this signal is captured by a camera and transferred to a computer for analysis (Drexler and Fujimoto; Huang et al.). The OCT laser light is reflected differently by the layers of penetrated retinal tissue and therefore, the scan enables histology-like examination of retinal structures in-vivo. This has multiple applications and is used in clinical routine or experimental eye research. Only few investigations to date determine various morphological properties of the fovea and the macula region based on accurate automated OCT measurements.

In clinical routine, the only commonly derived measure of OCT based images is retinal thickness. Specifically, the central retinal thickness (CRT) is employed for longitudinal follow-up of various retinal diseases and it remains an important marker for initial diagnosis. Most commonly, central foveal subfield thickness (CFST) is determined, defined as the mean thickness within a 1 mm circle centered by fixation close to the foveal minimum (Early Treatment Diabetic Retinopathy Study Research Group). A different definition of retinal thickness is to employ the minimal thickness derived at the thinnest part of the fovea ($\mathrm{CRT}_{\mathrm{min}}$).

So far, normal databases for retinal thickness suffer from different degrees of inaccuracy. OCT devices from different manufacturers can produce significantly different retinal thickness measurements (Wolf-Schnurrbusch et al.). Although conversion between devices is possible (Krebs et al., b,a), it is vitally important to correctly adjust the measurement region to obtain accurate and reproducible results (Heussen et al.). These might be reasons, why the full potential to use central retinal thickness as an early indicator of developing retinal abnormalities has so far not been employed.

Previous studies have shown that men had greater retinal thickness than women. Wagner-Schuman et al. assessed these gender differences on the same OCT device as the current study. They examined retinal thickness in nine fields, based on circular rings with 500 µm, 1500 µm and 3000 µm radius. Their CFST was measured as (264.5 ± 22.8) µm for men and (253.6 ± 19.3) µm for women ($p = 0.0086$) and they found significantly higher thicknesses in men for all but the superior outer and nasal outer EDTRS grid fields (Wagner-Schuman et al.). In an earlier study employing the same OCT device, mean CFST was (270.2 ± 22.5) µm with no difference in gender which is most likely due to by to the small cohort investigated. There, a mean CFST of (273.8 ± 23.0) in males and (266.3 ± 21.9) µm in females ($p = 0.1$) was found (Grover et al., b).

Some more detailed analyses of foveal pit morphology were recently carried out and various foveal characteristics have been proposed. Wagner-Schuman et al. employed a difference of Gaussians (DoG) model to determine foveal pit depth, diameter and maximum slope of 43 women and 47 men. They reported a foveal pit depth of (120 ± 27) µm and (119 ± 19) µm, a foveal pit diameter of (1930 ± 220) µm and (1960 ± 190) µm, and a maximum slope of $(12.2 \pm 3.2)°$ and $(11.8 \pm 2.2)°$ for men and women respectively.

Dubis and colleagues, who used a DoG model as well, presented the surface diameter of the foveal pit, which they defined as the distance from rim to rim. They presented the average diameter of six scans at 30° intervals obtained with 1940 µm for the Spectralis OCT (Dubis et al., b). Tick and colleagues (Tick et al.) have measured foveal pit diameter again derived from OCT images based on maximum rim height and found the diameter to be larger horizontally (2210 µm) compared to vertically (2450 µm).

Similar to the diameter, another approach is to investigate foveal radius which is usually defined as the distance from the foveal center to some outer boundary. Various definitions of radius and diameter regarding the foveal zone have been examined previously that are not necessarily relying on OCT data. O'Leary investigated foveal radius by using the commonly known kidney-shaped reflex of ophthalmoscopy in 20 myopic subjects (12 female, 8 male) and found the radius of young myopic subjects to be 1040 µm to 1700 µm . Delori et al. and colleagues measured the size of the reflex of the ring illumination of the fundus camera and listed the size of the reflex in 18 subjects (8 female, 10 male) to be larger in women than in men ($(0.27 \pm 0.07)°$ and $(0.16 \pm 0.04)°$, respectively; $p < 0.001$), which they gave to equivalent to 1190 µm and 744 µm respectively. However, such measurement is confounded by factors such as axial length as pointed out by Provis et al.. Yuodelis and Hendrickson investigated the rod free zone of the human fovea to be 650 µm to 700 µm (683 µm were measured in an adult specimen). Chui et al. found individual variations in the diameter of the foveal avascular zone (FAZ) when imaging the microvascular structure in vivo by adaptive optics scanning laser ophthalmoscope (AOSLO). They established a horizontal FAZ diameter of (607 ± 217) µm micrometer and a vertical FAZ diameter of (574 ± 155) µm. Dubis et al. (a) listed the FAZ diameter to range from 200 µm to 1080 µm, again based on AOSLO measurements. In the same work, Dubis

et al. (a) extracted foveal pit metrics from OCT derived data, and found the diameter to be 1120 µm to 2400 µm. Another work by Chen et al. investigated a "floor-diameter of the foveal pit" which they defined as the region where the retinal thickness "remained at a minimum", based on data obtained by the OCT device software. It was found that the average diameter of the foveal floor was (120 ± 40) µm and (150 ± 50) µm for the right and left eye respectively. This finding, however, depends on the resolution of the OCT since the fovea itself is a continuous pit with exactly one minimum. Therefore, such a definition of a foveal floor will be affected by an arbitrarily chosen tolerance that is used to determine the floor size around the foveal minimum.

Generally speaking, the size of the foveal radius, i.e. the size of the foveal pit diameter, is of great importance, because it describes the size of an area of best resolution in the eye. However, the size of the fovea is potentially physiologically constrained, possibly related to pupil size to achieve angular resolution (see (Provis et al.) and (Franco et al.)). Even though, visual resolution is not attributable to a single factor, it could be speculated that the size of the foveal radius may be correlated to visual performance indicators obtained.

Beside the size of the foveal zone, the slope of the foveal pit is another characteristic that is of historical importance as very early research connected it to visual acuity. According to Walls the optical effect of the slope of the deep convexiclivated fovea of some birds leads to local magnification at retinal photoreceptor level. This is supposed to be a result of the very steep fovea and a slight difference in refractive indices of vitreous humor and retina according to Valentin. Although humans do not possess such extreme foveas, it was recently suggested, that this optical effect could be extended to primate/human foveas (Reichenbach et al.).

The development of the foveal pit in children, and the maturation of human fovea in general, is a related interesting topic that relies on the analysis of foveal characteristics (Yanni et al.; Vajzovic et al.). It has already been demonstrated that there exists a significant difference in slope as well as in other characteristics between the foveal pits of preterm children and full-term controls (Yanni et al.). A rigorous investigation of the spectrum of foveal slopes in one subject or in different subject groups is therefore of high interest.

Closely related to slope and radius is the foveal rim height, h_{rim}, which is the retinal thickness at the top of the rim. Although a prominent rim might not be visible in all foveas, it is widely accepted that there is a point of largest retinal thickness outside the pit. Sigelman and Ozanics measured the retinal thickness at its maximum point at the foveal rim to be 230 µm based on histological preparations (shrinkage factor). Newer data exists by Ahnelt who measured the retinal thickness at the foveal rim to be 320 µm in a light microscopy image with little shrinkage artifacts. His material was well fixed and of quality suitable for electron microscopy without postmortem delay (Ahnelt).

Tick et al. derived the maximal retinal thickness in superior (S), inferior (I), nasal (N) and temporal (T) locations and found that (306 ± 16) µm was significantly lower on the temporal side, whereas the other locations were similar (S: (332 ± 16) µm , I: (325 ± 15) µm, N: (329 ± 17) µm).

The current investigation aims to provide a clear definition of five intuitive foveal characteristics that are derived from the mathematical fovea model introduced in Scheibe et al.. The presented characteristics include (1) mean retinal thickness inside a defined radius, (2) foveal bowl area, (3) a definition of foveal radius, (4) maximum foveal slope, and (5) the maximum height of the foveal rim. While mean retinal thickness is a characteristic of the eye as a whole, the remaining four characteristics are available in each modeled direction. As will be shown, there are significant differences when these properties are evaluated in different directions inside the same fovea. Therefore, an important aspect will be to highlight the asymmetric structure of the foveal region and discuss possible explanations for varying foveal characteristics.

At first, a compact computation scheme will be presented that shows how the CFST can directly be extracted for a modeled eye. Since the $\mathrm{CRT}_{\mathrm{min}}$ in the center of the fovea is an intrinsic part of the modeling procedure, this property will be analyzed as well and compared to earlier published results.

As a second fovea property, foveal bowl area, A_{bowl}, is introduced which can be calculated as an analytic integral equation of the model formula. This bowl area will then be used to derive a foveal radius that is superior to the usage of the foveal rim as boundary for the pit. These two characteristics will serve here to show the strong correlation of right and left eye within one subject.

Finally, the foveal slope and rim height characteristics, both already introduced in (Scheibe et al.), will be

investigated further. The slope will be examined for correlations to the foveal radius in different directions. Similar, the rim height will be used to reveal directional difference between male and female subjects.

Beside a rigorous discussion and comparison of our findings with available literature, the key point of the current work will be the analysis of the asymmetric structure of human foveas.

2. Materials and methods

To calculate the results presented here, 220 strictly controlled normal caucasian subjects of European descent were employed (Zocher et al.). From the 220 patients both eyes were scanned, but 31 OCT scans needed to be discarded for bad quality and therefore, a total of 409 OCT scans were analyzed. For 19 subjects only the right scan and for 12 subjects only the left scan was available, i.e. 208 right eyes and 201 left eyes were in this sample.

The data presented are based on 109 men and 111 women aged 21 years to 77 years with a mean/SD of (43 ± 13) years and (44 ± 14) years, respectively. The following number of men and women were within the following age decade brackets: 20 year-decade: 25 men and 25 women, 30 year-decade: 21 men and 18 women, 40 year-decade: 29 men and 28 women, 50 year-decade: 19 men and 22 women, 60 year-decade: 12 men and 16 women, and 70 year-decade: 3 men and 2 women.

Refractive error was distributed in a range of -9 D to 6 D with a mean/SD for men of (-1.04 ± 2.24) D and women of (-0.631 ± 2.250) D. Women and men showed no significant differences in ametropia ($p = .108$). Refraction was quantified based on the sphere obtained during best corrected subjectiv refraction. This spherical refractive error was more hyperopic as expected with age (men: $r = 0.321$, $p < .001$, women: $r = 0.39$, $p < .001$). Axial length was distributed between 20.8 mm to 27.6 mm with a mean/SD of (24.30 ± 1.02) mm for men and (23.40 ± 1.01) mm for women. A more detailed statistic of the sampled eyes properties can be found in table 1. The research followed the tenets of the Declaration of Helsinki for the use of human subjects.

eye	age	AL	BCVA	SE	S
right	42.6 ± 13.6	23.8 ± 1.12	-0.119 ± 0.0862	-0.523 ± 2.18	-0.823 ± 2.24
left	42.7 ± 13.6	23.8 ± 1.13	-0.125 ± 0.0774	-0.553 ± 2.19	-0.824 ± 2.23

Table 1: Properties of subjects' right and left eyes given as mean and standard-deviation. The table shows age (in years), axial length (AL in mm), best corrected visual acuity, which is the visual acuity in logMAR achieved with the optimal refractive correction in place (BCVA in logMar), spherical equivalent (SE in D), and sphere (S in D).

All datasets were captured with a Spectralis OCT (Heidelberg Engineering, Heidelberg, Germany) where each volume scan consisted of 97 B-Scans (at 512 A-Scans/B-Scan) and every A-Scan consists of 496 samples. For each OCT scan, an angle of 20° in both, x- and y-direction was used. The resulting exact metric dimension in x- and y-direction depend on the subject's specific eye parameters, but, approximately, each dataset represents a scanned volume of 6 mm × 6 mm × 1.92 mm.

The correct OCT image magnification was calculated, taking into account the subject's anterior corneal radius (mean of steep and flat meridian) and the focus obtained during measurement. These values were used to follow the approach given in the work of Garway-Heath et al..

All calculations necessary for the modeling and all statistics were carried out with Wolfram *Mathematica* (Wolfram Research), Version 10.3. To import the scanned volumes into *Mathematica*, the datasets were saved from the Spectralis OCT using the *raw data export* functionality. To read the binary format into *Mathematica*, an import software has been developed that is freely available from `github.com/halirutan`.

2.1. Fovea Analysis

The analysis in this work uses a fovea model function $\mathcal{M}$ with four free parameters μ, σ, γ, and α that was introduced in Scheibe et al.:

$$\mathcal{M}(r; \mu, \sigma, \gamma, \alpha) = \mu\sigma^2 r^\gamma \cdot \exp\left[-\mu r^\gamma\right] + \alpha\left(1 - \exp\left[-\mu r^\gamma\right]\right). \tag{1}$$

After importing the OCT volumes, the mode-parameters were calculated as described there using a model fit with a maximal model radius $r_{\max} = 2\,\text{mm}$ and with the following model parameter ranges: $\mu \in (0, 10]$, $\sigma \in (0, 2]$, $\gamma \in (1, 10]$ and $\alpha \in [-2, 2]$. For each eye 40 equally distributed angular directions were fitted.

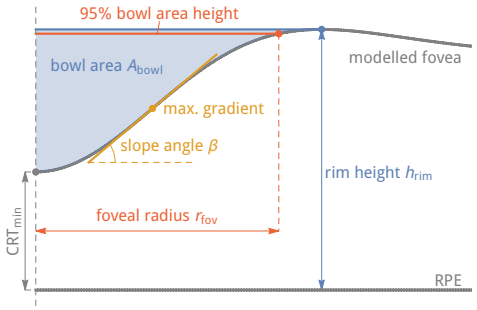

Figure 1: The foveal characteristics used in this publication can be calculated automatically for each eye with the given approach. The CRT_{min} represents the minimal height between the RPE and ILM which is defined as the center of the fovea. All radially modeled fovea forms have this central point in common. The rim height $h_{\text{rim}}$is the distance between RPE and the model function at the foveal rim top. This maximum point of the rim is unique and exists in every model function. The blue region is the area between the model function and a horizontal line that connects with the maximum rim point. It represents the foveal bowl A_{bowl} and its value can be calculated as shown in section 2.1.2. The point of maximal gradient that always exist between the fovea center and the rim defines the slope angle β. The foveal radius is defined by the point, where the bowl is filled with 95 % of its area.

The model-parameters for each subject were then employed to calculate fovea characteristics that allow for a detailed and intuitive analysis. Some of the used foveal characteristics were already presented in (Scheibe et al.), others will be explained below. In general, the presented foveal properties can be divided into two groups. The first group consists of characteristics that are defined for each eye and characterize one specific value for the fovea as an entity, while the second group are characteristics defined for each of the 40 fitted directions per fovea.

The minimal central retinal thickness (CRT_{min}) and the mean retinal thickness (CFST) inside the 1 mm circle centered on the foveal minimum are defined once per fovea and thus fall within the first group. Note that although the CRT_{min} value serves as center of the fovea model, it is basically unrelated to the model fit procedure, because its value, the distance between ILM and RPE in the foveal center, is directly extracted from OCT.

The remaining 4 foveal characteristics used in this work are calculated for each fitted direction. Later, either median values of the 40 directions will be analyzed or values of the anatomical directions nasal, temporal, inferior, and superior will be compared. Characteristics that are available for each fitted direction are the foveal bowl area (A_{bowl}), the foveal radius (r_{fov}), the maximal slope inside the foveal pit (slope), and the retinal thickness of the foveal rim (h_{rim}). All these properties are depicted in figure 1.

The definition of the foveal slope angle β and the rim height h_{rim} was already given in Scheibe et al. and the exact formulas are not repeated here; nevertheless, a short description will follow. Due to the structure of the model formula, the maximum slope angle β can easily be calculated by evaluating the gradient of the model function $m = \partial_r \mathcal{M}(r)$ at the first inflection point. To transform the result to degree the transformation $\beta = 180° \cdot \arctan(m)/\pi$ can be applied.

The foveal rim is the highest point of a fovea and is a unique maximum of the model formula. Its position r_{rim} can be calculated through the first derivative of the model function by solving $\partial_r \mathcal{M}(r; \mu, \sigma, \gamma, \alpha) = 0$ for r. This gives

$$r_{\text{rim}} = \left(\frac{\alpha + \sigma^2}{\mu \sigma^2} \right)^{\frac{1}{\gamma}} \tag{2}$$

and the overall rim height h_{rim} can be obtained by the sum of CRT_{min} and $\mathcal{M}(r_{\text{rim}})$.

2.1.1. Central Foveal Subfield Thickness (CFST)

Clinically it has been common to employ a nine-field grid to examine retinal thickness. These circular rings with 500 µm, 1500 µm and 3000 µm radius were originally defined for examination of fundus images by the ETDRS group (Early Treatment Diabetic Retinopathy Study Research Group). The grid fields of retinal thickness generally divide the $\approx 20°$ macular region into sections where the retinal thickness is measured and compared. Commonly, the central circle of the ETDRS grid within 1 mm diameter is the measure investigated and it is defined as central foveal subfield thickness (CFST). If the measurement region is centered correctly, the CFST is an important foveal characteristic with the foveola in its center.

To calculate CFST from OCT data, one has to uniformly distribute a number of sampling points inside this 1 mm circle. The CFST is then given by the mean of all retinal thickness values at these sampling points. In OCT data, the most direct approach for this is to use all A-scans that fall within the 1 mm circle as sampling points.

However, in this work, a fovea is represented by a number of radial model functions centered in the foveola and therefore, a different method is required to approximate uniform sampling. The key idea is instead of sampling OCT data in x- and y-direction, to use a radial sampling that covers the inner 1 mm circle by varying angles φ and radii r. Since each fovea was modeled in 40 equally spaced directions, only fixed sampling for φ is available and, therefore, φ cannot be chosen freely. Along each one of the 40 model functions, $\mathcal{M}(r)$ can be evaluated for arbitrary values of r.

To achieve a uniform distribution inside the circle, every sampling point should cover the same area-fraction. As depicted in figure 2(a), in the built-in CFST of the OCT software tool employs the following paradigm: every sampling point covers a small rectangular area of the same size that is surrounded by gray grid lines.

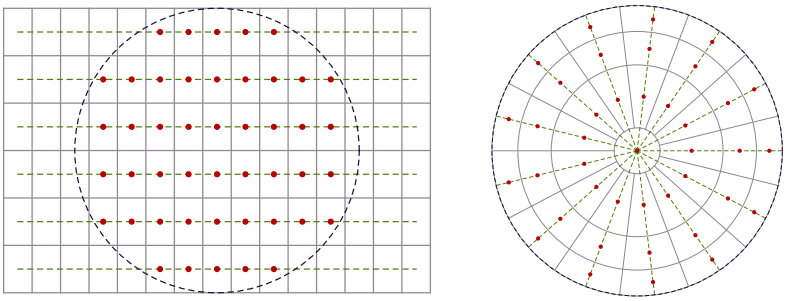

(a) (b)

Figure 2: Distribution of sampling points to calculate the CFST. Sampling points are depicted as red dots inside a gray grid, dividing the area in equally sized partitions. In the left figure, a possible distribution is given that uses the underlying OCT B-scans, drawn as green, dashed lines. All red sampling points are equally spaced along a B-scan and need to lie inside the 1 mm circle. In right figure, one possible distribution of sampling points is shown that can be used, when retinal thickness is only available on radial model functions (depicted as green, dashed lines). Like in figure (b), each small partition surrounded by gray lines has the same size.

In figure 2(b), a different partition of the 1 mm circle is depicted, which shares the property that all gray areas containing a sampling point have the same size. Additionally, it is easily possible to construct this partition to make all sampling points lie on the green dashed lines that represent the model-function in all directions.

The partition shown in 2(b) can be derived from a recurrence equation to obtain the gray circles that are required to ensure all small sampling areas are of the same size:

- Given the number of modeled directions n_d, the number of different radial sampling points n_r that can be chosen freely, and with one additional central sampling point, the overall number of red points is $n = n_d \cdot n_r + 1$.

- With n given, the area of one small partition can be calculated by dividing the area of the measurement region, A_{CFST}, into n equal partitions by $A_0 = A_{\mathrm{CFST}}/n = 2\pi r_{\mathrm{CFST}}^2$. To obtain the usual definition of 1 mm circle CFST, $r_{\mathrm{CFST}} = 1/2$ mm. Therefore, the radius, r_0, of the central gray circle in 2(b) is given by $r_0^2 = A_0/\pi$.
- The area of the annulus between two adjacent radii r_n and r_{n+1} is simply $n_d \cdot A_0$ since each ring consists of n_d segments that have the same size A_0. Additionally, taking the standard definition of an annulus, its area can be calculated by the difference of two disk with radii r_{n+1} and r_n which leads to the recurrence equation
$$n_d \cdot A_0 = \pi r_{n+1}^2 - \pi r_n^2, \quad r_0^2 = A_0/\pi$$
- By solving the above equation for r_{n+1}^2 and expanding some of the recursive steps, one finds the explicit solution for the i-th radius to be
$$r_j^2 = r_{\mathrm{CFST}}^2 \left(\frac{j \cdot n_d + 1}{n_d \cdot n_r + 1} \right), \quad j = 0, \ldots, n_r$$
Note that r_{n_r} is simply r_{CFST} and that sampling points were placed in the middle between two neighboring radii.

Given the list of radii r_j, the final approximation of the CFST using our model is given by

$$\mathrm{CFST} = \mathrm{CRT}_{\min} + \frac{1}{n} \sum_{i=1}^{n_d} \sum_{j=0}^{n_r - 1} \mathcal{M}_i \left(\frac{r_j + r_{j+1}}{2} \right), \tag{3}$$

where $\mathcal{M}_i$ denotes the model-function in the i-th direction. Readers should note that this is only one possible approximation of CFST using radial model functions and that different sampling, interpolating and integrating schemes can be derived as well.

2.1.2. Foveal Bowl Area

The bowl area is the blue region depicted in figure 1 and it is defined as the area enclosed by the horizontal line to the highest point on the foveal rim and the model function.

To calculate an analytic formula for this area, the point $(r_{\mathrm{rim}}, \mathcal{M}(r_{\mathrm{rim}}))$ (see equation 2) is required. The rectangular area under the horizontal upper boundary line of the foveal bowl is given by the product of r_{rim} and $\mathcal{M}(r_{\mathrm{rim}})$. Using this, the foveal bowl area can be given as the difference

$$A_{\mathrm{bowl}} = r_{\mathrm{rim}} \cdot \mathcal{M}(r_{\mathrm{rim}}) - \int_0^{r_{\mathrm{rim}}} \mathcal{M}(r) dr \tag{4}$$

An analytic solution to equation 4 is possible, but, due to its length, cannot be presented here.

2.1.3. Foveal Boundary Radius

The foveal radius was derived from the model formula to obtain a boundary for the foveal pit. While it seems natural to use the highest point on the foveal rim, r_{rim}, for this purpose, it would come with a drawback, because, although most foveal shapes have a clear rim, it is possible to observe foveas where the rim is almost even. Such foveas, although they possess a *rim point*, possibly have this point at a significantly greater distance to the foveal center, compared to a fovea with similar properties alongside a more defined rim structure. That would lead to a foveal radius definition with a high variance, even when the foveal structures itself share many other characteristics.

It was found that the foveal bowl area, which includes r_{rim} only indirectly as integration boundary, can be used to obtain a very consistent measure for the foveal radius. For this purpose, a defined percentage p (usually 95 %) of the foveal bowl area is used which is determined by where the foveal form is hit if the bowl would be *filled* with the reduced area only. In figure 1 this is exemplary shown by the red $p = 95\,\%$ line and the distance between foveal center and the red dot on the fovea shape.

Following the same argumentation as in section 2.1.2, the foveal radius r_{fov} can be obtained by solving the following equation

$$r_{\mathrm{fov}} \cdot \mathcal{M}(r_{\mathrm{fov}}) - \int_0^{r_{\mathrm{fov}}} \mathcal{M}(r)dr = p \cdot A_{\mathrm{bowl}} \tag{5}$$

In this work, numeric solutions to equation 5 were obtained by a simple bisection algorithm to find the root. This approach is justified due to the very nature of the expression, because equation 5 will have exactly one solution in the interval $0 < r < r_{\mathrm{rim}}$ when the percentage is between 0 % and 100 %.

3. Results and Discussion

The 409 available data-sets consisted of 208 right and 201 left, and 207 female and 202 male eyes respectively. The distribution per decade (20 to 80 years of age) was chosen based on the age and gender distribution of Leipzig, Germany (census data) and it included solely caucasian subjects. For each eye 40 equally angular distributed radial fovea fits were calculated, resulting in a total of 16360 foveal model shapes. The overall root mean square fit error was $(3.01 \pm 1.09)\,\mu\mathrm{m}$.

Basing on the model-parameters μ, σ, γ, and α, the derivation of five useful foveal characteristics was presented: (1) the maximum foveal slope, (2) the area inside the foveal bowl, (3) a foveal radius, (4) the maximum hight on the foveal rim, and (5) the central foveal subfield thickness. The introduced characteristics, that are partly known from literature with varying definitions, have now a formal definition on the basis of the fovea model introduced in Scheibe et al.. A need for such a "consensus on the terms and methods used to define the different features of foveal morphology" was postulated previously by Provis et al.. Once a unified terminology is established, subsequent investigations into the morphology of foveae in humans and other species will work on a common ground and results will be better comparable.

Table 3 shows the mean/SD values of all obtained model parameters and foveal characteristics. For each presented property the median value of all fitted 40 directions and the values in four the anatomical directions nasal, temporal, inferior and superior are given. Additionally, each row is divided into right and left eye to make a direct comparison possible. Finally, the table is divided into three large blocks presenting all, male and female subjects separately. In addition to table 3, mean/SD values of CFST and $\mathrm{CRT}_{\mathrm{min}}$ split by gender and eye position are given in table 2.

Figure 3 shows examples of foveas that exhibit extreme values in particular foveal characteristics. The selected OCT images are the central scans through the fovea and show the nasal and temporal direction. The mean value of both directions was taken to select examples that possess the largest and smallest values in the specific characteristic. The single images show the following characteristics: 3(a) and 3(b) foveal slope with 5.1° and 16.9° respectively, 3(c) and 3(d) foveal bowl area with $0.025\,\mathrm{mm}^2$ and $0.098\,\mathrm{mm}^2$ respectively, 3(e) and 3(f) foveal radius with 0.72 mm and 1.23 mm respectively, and 3(g) and 3(h) foveal rim height with 290.4 µm and 392.8 µm respectively.

In the following sections, the data presented in summarized form in table 2 and 3, will be combined and discussed in different ways to illustrate inter-relationships.

3.1. Correlation between right and left eye

One compelling topic is the correlation between a subject's right and left eye. Regarding a specific research question, it would theoretically be possible to double a studies sample size by using both eyes in an analysis. For this, both eyes must be statistically independent. Merely the fact that both eyes are from the same person disqualifies them as being as diverse as two single eyes from two independent observers. On the other hand, there might be research questions that focus on specific problems where corresponding eyes might indeed be regarded as uncorrelated in some sense. In general, an existing correlation between right and left eye of the same subject is often inevitable and therefore, a usage of all eyes in e.g. a statistical test is not allowed. A detailed discussion about this topic can be found e.g. in Armstrong.

For the current work, the authors presumed that a correlation between right and left eyes most likely appears in foveal characteristics which include information about the absolute size. Therefore, the foveal

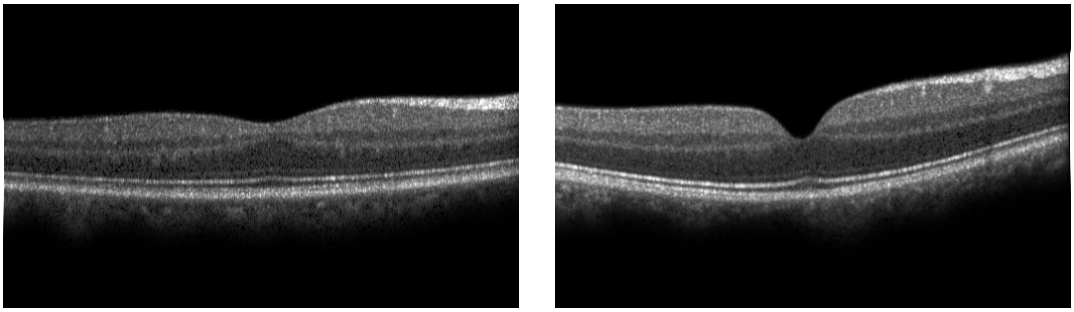

(a) flat foveal slope

(b) steep foveal slope

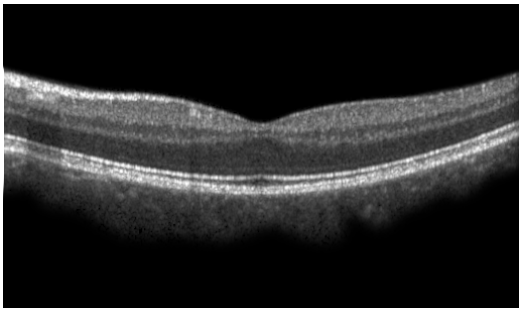

(c) small foveal bowl area

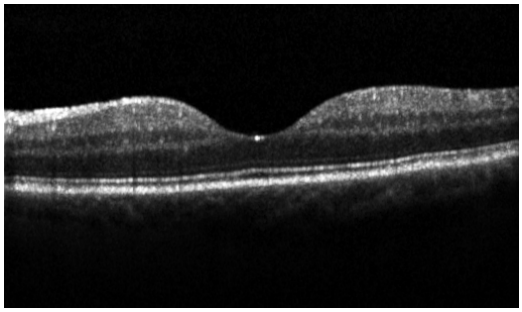

(d) large foveal bowl area

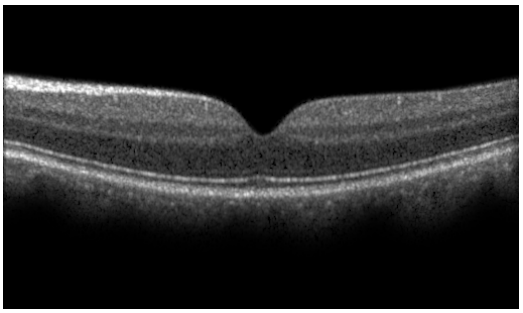

(e) small foveal radius

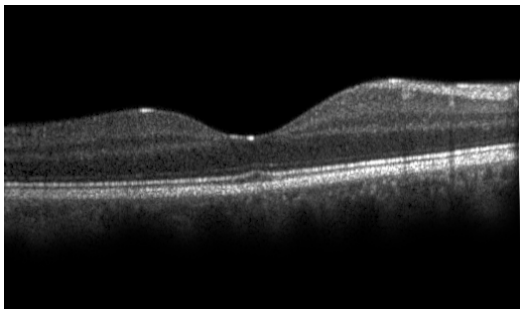

(f) large foveal radius

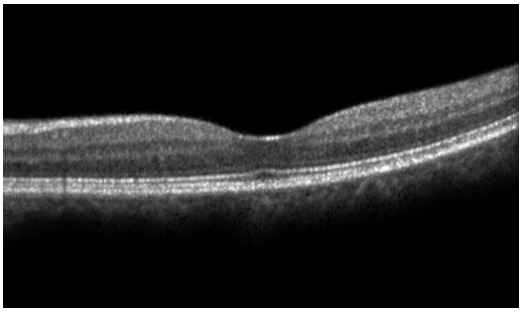

(g) small foveal rim height

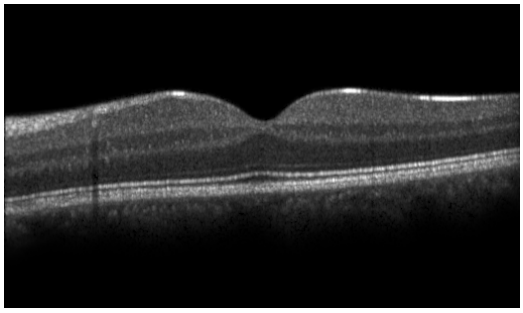

(h) large foveal rim height

Figure 3: Selected OCT scans to illustrate extreme foveal characteristics. While the left column displays minimal values, the right column shows maximum values of the specified characteristic. From first to last row the pairs demonstrate extreme examples for foveal slope, bowl area, radius, and rim height respectively. Each image shows the central OCT scan through the fovea. The mean values (from nasal and temporal direction depicted) of the shown fovea are: for the foveal slope (a) 5.1° and (b) 16.9°, for the foveal bowl area (c) 0.025 mm^2 and (d) 0.098 mm^2, for the foveal radius (e) 0.72 mm and (f) 1.23 mm, and for the foveal rim height (g) 290.4 µm and (h) 392.8 µm.

radius r_{fov} and the foveal bowl area A_{bowl} were chosen to compare eyes within the same subject, where right and left eye were available. Figure 4 contains the scatter-plots of these correlations that show a striking connection between right and left eyes. Both, the foveal radius and the foveal bowl area possess high correlations of $r = 0.924$ ($p < .001$) and $r = 0.959$ ($p < .001$) between right and left eyes respectively.

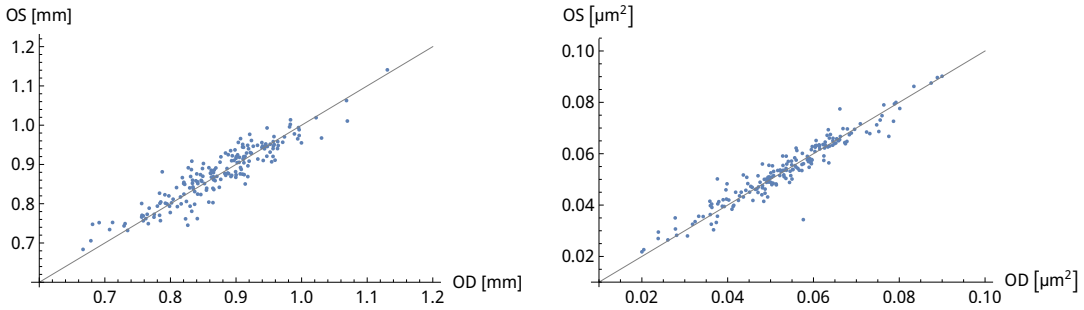

(a) foveal radius ($r = 0.924$)

(b) foveal bowl area ($r = 0.959$)

Figure 4: Scatterplots for two different foveal characteristics showing the correlation between right and left eyes. The plots clearly show that right and left eyes are highly correlated for the foveal radius ($p < .001$) and bowl area ($p < .001$). Both characteristics are considered to be directly correlated to the overall size of the eye.

The consequence of this is that one has to be extremely cautious when mixing both, right and left eyes into the same sample group. If in doubt, it is advised to stick to the common rule of using only one eye per subject (e.g. right eye) as it is done in many studies. For the current work, the tables and analyses are given for the respective eye independently and if eye position is not specified, only right eyes were compared.

Apart from showing inter-subject correlations, characteristics like the foveal bowl area and the radius have many further application domains. Clinically, an exact description and measurement of bowl area is useful in detection of vitreomacular interface pathology, for example macular hole development. Different types and stages of macular holes exist, each of which will affect the bowl area parameter, beginning with foveal detachment (stage 1), partial thickness holes (stage 2) and full thickness holes (stage three). Epiretinal membranes which may develop pseudoholes can also be identified by the bowl area parameter. Potentially, the bowl area parameter can only be measured in early stages, as the model used here can only successfully deal with stage 1 holes. This has to be investigated in a subsequent study. However, as the potential key application is early diagnosis of new cases or beginning fellow-eye involvement, the paradigm presented will produce highly accurate results where they are needed most.

Macular holes caused by persistent adherence of the cortical vitreous to the fovea with adjacent vitreoretinal separation, often begin gradually and are associated with visual acuity reduction, metamorphopsia, and a central scotoma. Fellow-eye involvement has been shown to affect 21 % of unilateral cases (Duker et al.) or was shown to newly develop in 13 % of eyes within 48 months (Benson et al.). Cross-sectional OCT images provide information on the vitreomacular interface not visible with biomicroscopy, information is obtained on the pathogenesis, classification, and diagnosis of macular hole. In addition, the OCT has been employed to measure the hole diameter as average of vertical and horizontal diameter, determined at the minimal extent of the hole (Kang et al.). In a different application, the OCT is used to identify the anatomical status after macular hole surgery by an *adjusted* hole size parameter which is defined as the ratio between the hole size and the fellow eye's *foveolar floor* size (distance between the boundaries free of ganglion cell layer) (Shin et al.).

The novel assessment based on the parameters of this paper enable scientists and clinicians alike to assess hole formation on a new level of accuracy. The hope is that by quantifying even small deviations from the norm, a better grading and an earlier detection of hole formation is possible.

3.2. Retinal thickness differences between male and female subjects

CFST has been investigated in the past and, although, some studies generalize this to be central retinal thickness (CRT), the current study will not employ the latter term as it can easily be confused with CRT_{min},

which is a second meaningful measurement representing the deepest part of the foveal pit. Therefore, CRT_{min} is the minimal retinal thickness, which is the location the ETDRS grid should be centered on.

Central foveal subfield thickness has been defined within other populations on the same OCT device. Heussen et al. measured CFST to be 278.9 µm for the device's automatic measurement mode. Wolf-Schnurrbusch and colleagues established 289 µm (Wolf-Schnurrbusch et al.) in their population, while Grover and associates found the CFST to be (271.4 ± 19.6) µm (Grover et al., a). A difference in retinal thickness between male and female subjects was already reported in different studies (Kirby et al.), however some of the research findings (Delori et al.) were potentially established due to confounding factors (e.g. axial length (Provis et al.)). Previous gender related findings for CFST on the same OCT device also found smaller thicknesses for women (men: (264.5 ± 22.8) µm and women (253.6 ± 19.3) µm (Wagner-Schuman et al.), with $p = 0.0086$). Grover et al. (b) found no gender differences for CFST measured with the Spectralis OCT (men: (273.8 ± 23.0) µm and women (266.3 ± 21.9) µm, with $p = 0.1$), which can be attributed to insufficient sample sizes.

The current investigation established gender differences as depicted in Table 2 and Figure 5: The CFST is significantly larger in males than in females for both eyes ($p < .001$), but a significant difference in CRT_{min} between different gender could not be found (right eyes $p = .139$, left eyes $p = .308$).

		all	male	female
CFST [µm]	r	277.48 ± 19.817	282.74 ± 20.277	272.12 ± 17.897
	l	277.74 ± 19.702	282.58 ± 20.441	272.74 ± 17.659
CRT_{min} [µm]	r	229.67 ± 18.844	232.02 ± 20.402	227.27 ± 16.875
	l	230.00 ± 18.947	231.81 ± 20.305	228.14 ± 17.343

Table 2: The central foveal subfield thickness (CFST) and then minimal central retinal thickness (CRT_{min}) both in [µm] given as mean and standard-deviation for all subjects and divided by gender. Each row is split into right (r) and left (l) eyes. While the CFST is significantly larger in males than in females for both eyes ($p < .001$ both), a significant difference in CRT_{min} between different gender could be found (right eyes $p = .139$, left eyes $p = .308$). Note that the gender differences in CFST are still significant even if a correction for axial length was done.

With CRT_{min}, CFST, and h_{rim} (see table 3), a comprehensive comparison of three retinal thickness measures can be given. This leads to a greater insight, because as depicted in figure 5, foveal rim thickness values can be analyzed for different anatomical directions. The box-and-whisker diagram shows that there are clear differences between directions and that e.g. temporal rim heights are smaller than in any other directions ($p < .001$ for all in men and women). Regardless of the directional differences, female subjects show significantly smaller h_{rim} values in all four directions ($p = .002$, $p = .006$, $p = .001$, and $p = .03$ for the directions N, T, I and S respectively).

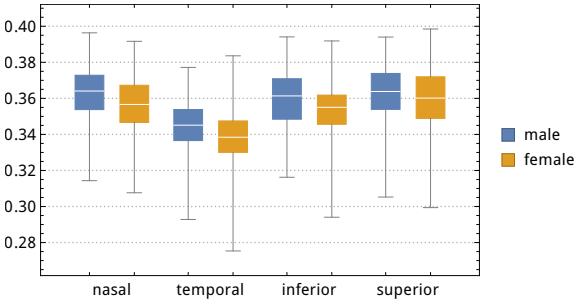

Figure 5: Rim height h_{rim} [mm] of male and female subjects divided into the four anatomical directions. Male rim heights are larger than female rim heights in each direction. The nasal, temporal, and inferior differences are significant ($p = .002$, $p = .006$, $p = .001$, and $p = .03$ resp). Noteworthy, in superior direction, the difference is statistically not as strong as in the other directions.

For the first time characteristics like h_{rim} can be calculated for various directions like presented here for nasal, temporal, inferior and superior directions. This sets a precedent in resolving structural variations and

since not only the four anatomical directions can be analyzed, but virtually every direction, novel findings like shown in figure 7 can easily be investigated.

The relationship of the presented h_{rim} with data in the literature is difficult to establish. A comparison of histology with OCT has previously been computed for a macaque fovea to aid conversion (Anger et al.), but relative shrinkage is likely depending on specific fixation and embedding protocols. Besides species specific proportions, individual variations have to be, at least in part, attributed to preceding preparatory influences. When manually measuring a histological fovea section of baboon tissue (Figure 6B of Krebs and Krebs), maximum rim height was 363 µm. For a human fovea, a maximum rim height was measured manually as 320 µm (left side of image) and 333 µm (right side of image), see Figure 6-91 of Fine and Yanoff. Published OCT data, for example in Figure 1 of Jonnal et al., gave 379 µm nasally and 347 µm on the temporal side of the horizontal scan depicted. Although this is only an individual scan (healthy subject "S3" of Jonnal et al., gender or age not given), this data is based on OCT, hereby facilitating comparison to the current data. Differences of this example image to the current model data presented in the next paragraph can be attributed to manual measurement from the published image versus model based computation, alongside individual variation with unknown gender or age information.

In this work, nasally, h_{rim} was 360 µm and significantly larger then temporally with 342 µm ($p < .001$). Men presented with larger maximum rim height compared to women (right eye: nasally 364 µm versus 357 µm with $p = .002$; temporally 345 µm versus 339 µm with $p = .001$).

3.3. Asymmetry of the foveal region

As already mentioned in the discussion so far, the human fovea is not a round and symmetric structure. When the foveal form along different (anatomical) directions is compared, the fovea presents itself as a highly varying structure that shows clear differences in all investigated characteristics. To our knowledge, a detailed investigation how important foveal characteristics depend on anatomical directions is not available so far.

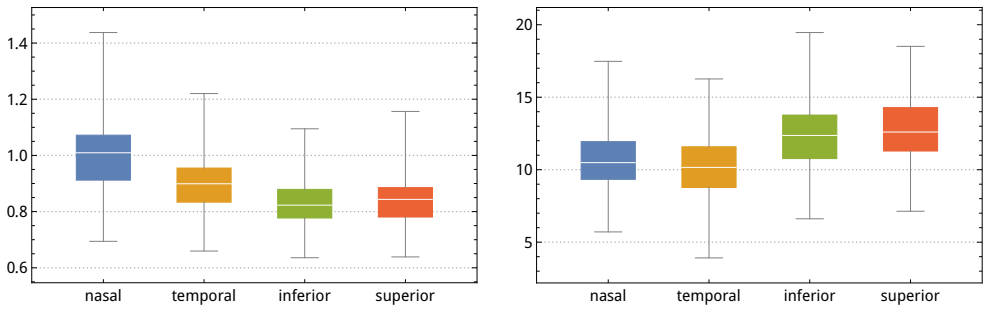

(a) foveal radius r_{fov} [mm] (b) foveal slope [°]

Figure 6: Asymmetries of foveal characteristics when viewed for different anatomical directions. The nasal radius is larger then all the other 3 directions ($p < .001$) and the temporal radius is larger than radii in inferior and superior direction ($p < .001$). A difference between the foveal radius in inferior and superior direction could not be shown ($p = 0.149$). The foveal slope in superior direction is larger than in nasal and temporal direction ($p < .001$ for both), but a significant difference to the inferior direction cannot be shown ($p = .107$).

Figure 6 reveals the dependency of foveal radius and slope angle on anatomical directions. The foveal radius is larger in nasal and temporal direction compared to inferior and superior position. This suggests that the fovea has an elliptic form with the larger axis along the nasal to temporal direction. Interestingly, the foveal slope shows a different behavior as the temporal direction has the smallest slope angle and both, inferior and superior angles are clearly larger than the others (p-values, see figure 6). This interesting finding can be better demonstrated when taking all modeled directions into account. Figure 7 shows a polar plot of the foveal radius and slope for all right eyes. With the current data, it can be shown that the foveal radius is inversely correlated with slope as a steeper slope will lead to a smaller radius and vice versa ($r = 0.408$

with $p < .001$). Such a demonstration of the asymmetry of the fovea has to the knowledge of the authors not been demonstrated so far.

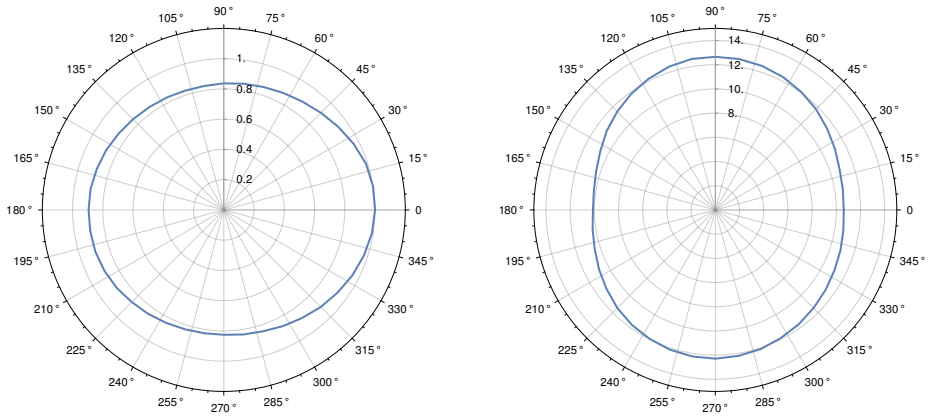

(a) foveal radius [mm]

(b) foveal slope [°]

Figure 7: Asymmetries of foveal radius and slope in a direct polar plot of all right eyes taking 40 modeled directions into account. Anatomical directions N, S, T, and I are represented by 0°, 90°, 180°, and 270° resp. Subfigure (a) shows the elliptic form of the foveal radius that has its largest extent along the N-T axis, although the ellipse appears to be slightly rotated. The foveal slope shows similar behavior, where the largest extend is along the I-S axis.

One possible explanation for this result is the influence of the retinal nerve fiber layer (RNFL) on the retinal thickness which in return influences the foveal slope. Nerve fibers running radially from the optic nerve toward the fovea arrive at the nasal side. There, they split up to run around the RNFL-free zone of the fovea until they are reunited at the temporal side. Whether this hypothesis contains some truth needs to be further investigated and discussed with experts in the field of foveal development.

4. Conclusion

The main goal of the current study was to present a detailed and accurate analysis of various fovea characteristics to reveal existing foveal variations and, above all, to expose the highly asymmetric form of foveas. Another purpose was to make the current analysis comparable to existing results which is one reason why computation schemes to commonly used characteristics like CFST were presented. In the case of CFST it was demonstrated that some researchers found similar results (Heussen et al.; Wolf-Schnurrbusch et al.; Grover et al., a), while others (Wagner-Schuman et al.) showed larger differences compared to the current study. In this work, previously published significant differences of CFST between men and women were also found. On the other hand, $\mathrm{CRT}_{\mathrm{min}}$ presented with no gender differences.

The presented results for the foveal slope showed general agreement with the results presented in Wagner-Schuman et al.; Dubis et al. (a). The vast improvement of the current results is that now it is possible to give a detailed analysis for various different directions. While Wagner-Schuman and colleagues showed a slope of $(12.2 \pm 3.2)°$ for men, in this study a great variance of more than 2° could be demonstrated in different anatomical directions (men right eye, N:10.8°, T:10.3°, I:12.6°, S:12.9°).

For characteristics like h_{rim}, a comparison to existing literature was difficult as analyses of larger subject groups could not be found. A comparison with histological examples disclosed that such data demonstrates h_{rim} to be about 40 µm smaller (Krebs and Krebs), while manual measurement of an OCT scan presented in a recent work (Jonnal et al.) was close to the results presented here. There seems to be a general consensus that the nasal h_{rim} is larger than temporal. However, an analysis as detailed as given in this work, taking all four directions into account, does not seem to exist so far.

Finally, figure 7 presents a way to unleash the full potential of such a detailed multi-directional analysis as described here. It is now not only possible to measure differences in a particular direction, with the method at hand, completely new approaches and insights become available. For instance, figure 7 raises interesting follow-up questions, e.g. how close the presented elliptic form is to a real ellipse and how differences could be explained. Another issue is that the ellipse-like shape seems to be slightly rotated. In the light of the fact that the optic nerve head is towards upper right position compared to the right eye fovea, one could ask the question whether the direction of the major axis is connected to the position of the optic nerve head.

		model parameters				foveal characteristics			
		μ	σ	γ	α	slope [°]	A_{bowl} [mm^2]	r_{fov} [mm]	h_{rim} [µm]
all subjects									
median	r	1.26 ± 0.185	0.472 ± 0.0378	1.68 ± 0.195	0.0610 ± 0.0319	11.5 ± 2.11	0.0537 ± 0.0130	0.874 ± 0.0772	357 ± 15.6
	l	1.26 ± 0.183	0.470 ± 0.0344	1.68 ± 0.190	0.0628 ± 0.0294	11.5 ± 2.10	0.0539 ± 0.0129	0.879 ± 0.0752	357 ± 15.6
nasal	r	1.10 ± 0.302	0.469 ± 0.113	1.67 ± 0.235	0.0593 ± 0.114	10.6 ± 2.04	0.0628 ± 0.0153	1.00 ± 0.110	360 ± 16.0
	l	1.19 ± 0.341	0.450 ± 0.0839	1.68 ± 0.224	0.0742 ± 0.0525	10.9 ± 2.09	0.0616 ± 0.0153	0.975 ± 0.108	361 ± 16.2
temporal	r	1.23 ± 0.271	0.451 ± 0.0550	1.66 ± 0.212	0.0518 ± 0.0361	10.1 ± 2.13	0.0486 ± 0.0127	0.894 ± 0.0933	342 ± 15.8
	l	1.14 ± 0.241	0.468 ± 0.0866	1.66 ± 0.223	0.0392 ± 0.0837	9.81 ± 2.00	0.0499 ± 0.0132	0.920 ± 0.0933	342 ± 15.6
inferior	r	1.30 ± 0.249	0.512 ± 0.0671	1.63 ± 0.204	0.0421 ± 0.0531	12.3 ± 2.29	0.0508 ± 0.0130	0.826 ± 0.0803	357 ± 16.3
	l	1.28 ± 0.240	0.516 ± 0.0638	1.63 ± 0.228	0.0396 ± 0.0511	12.3 ± 2.22	0.0506 ± 0.0127	0.827 ± 0.0784	357 ± 16.2
superior	r	1.43 ± 0.249	0.470 ± 0.0431	1.74 ± 0.220	0.0721 ± 0.0306	12.7 ± 2.30	0.0549 ± 0.0137	0.837 ± 0.0822	362 ± 16.5
	l	1.43 ± 0.244	0.466 ± 0.0439	1.74 ± 0.196	0.0747 ± 0.0328	12.6 ± 2.37	0.0554 ± 0.0135	0.843 ± 0.0773	363 ± 16.5
male									
median	r	1.26 ± 0.194	0.484 ± 0.0410	1.62 ± 0.177	0.0562 ± 0.0345	11.8 ± 2.16	0.0523 ± 0.0124	0.861 ± 0.0809	360 ± 14.7
	l	1.26 ± 0.195	0.482 ± 0.0328	1.62 ± 0.171	0.0593 ± 0.0308	11.8 ± 2.03	0.0528 ± 0.0125	0.864 ± 0.0778	360 ± 15.1
nasal	r	1.07 ± 0.312	0.494 ± 0.142	1.60 ± 0.220	0.0419 ± 0.154	10.8 ± 2.16	0.0613 ± 0.0145	0.993 ± 0.104	363 ± 15.6
	l	1.19 ± 0.399	0.464 ± 0.0927	1.62 ± 0.216	0.0693 ± 0.0526	11.2 ± 2.03	0.0605 ± 0.0148	0.966 ± 0.106	365 ± 16.3
temporal	r	1.24 ± 0.314	0.459 ± 0.0667	1.62 ± 0.210	0.0481 ± 0.0387	10.3 ± 2.16	0.0475 ± 0.0127	0.884 ± 0.105	345 ± 15.1
	l	1.14 ± 0.275	0.486 ± 0.102	1.60 ± 0.212	0.0290 ± 0.109	10.1 ± 1.97	0.0490 ± 0.0129	0.905 ± 0.0998	346 ± 14.8
inferior	r	1.29 ± 0.265	0.531 ± 0.0774	1.58 ± 0.200	0.0321 ± 0.0640	12.6 ± 2.39	0.0494 ± 0.0124	0.813 ± 0.0806	361 ± 15.7
	l	1.28 ± 0.263	0.530 ± 0.0638	1.56 ± 0.211	0.0330 ± 0.0559	12.6 ± 2.16	0.0490 ± 0.0124	0.813 ± 0.0837	360 ± 15.6
superior	r	1.46 ± 0.243	0.477 ± 0.0437	1.70 ± 0.194	0.0692 ± 0.0308	12.9 ± 2.28	0.0528 ± 0.0128	0.816 ± 0.0800	364 ± 15.4
	l	1.44 ± 0.244	0.474 ± 0.0431	1.70 ± 0.182	0.0723 ± 0.0324	12.9 ± 2.29	0.0542 ± 0.0129	0.829 ± 0.0783	366 ± 15.2
female									
median	r	1.26 ± 0.176	0.460 ± 0.0294	1.73 ± 0.198	0.0659 ± 0.0282	11.3 ± 2.04	0.0552 ± 0.0135	0.887 ± 0.0712	354 ± 15.9
	l	1.26 ± 0.171	0.457 ± 0.0317	1.74 ± 0.192	0.0664 ± 0.0275	11.3 ± 2.14	0.0550 ± 0.0133	0.893 ± 0.0699	354 ± 15.7
nasal	r	1.13 ± 0.289	0.444 ± 0.0654	1.75 ± 0.228	0.0771 ± 0.0413	10.5 ± 1.90	0.0643 ± 0.0159	1.01 ± 0.117	357 ± 15.7
	l	1.19 ± 0.270	0.435 ± 0.0713	1.75 ± 0.217	0.0793 ± 0.0522	10.7 ± 2.13	0.0626 ± 0.0159	0.985 ± 0.111	357 ± 15.4
temporal	r	1.21 ± 0.220	0.443 ± 0.0387	1.71 ± 0.205	0.0557 ± 0.0330	9.91 ± 2.08	0.0497 ± 0.0126	0.905 ± 0.0784	339 ± 15.9
	l	1.13 ± 0.202	0.449 ± 0.0620	1.72 ± 0.220	0.0498 ± 0.0426	9.51 ± 2.00	0.0509 ± 0.0134	0.935 ± 0.0840	339 ± 15.7
inferior	r	1.31 ± 0.233	0.493 ± 0.0480	1.69 ± 0.192	0.0523 ± 0.0367	11.9 ± 2.14	0.0522 ± 0.0135	0.838 ± 0.0783	354 ± 16.1
	l	1.28 ± 0.216	0.502 ± 0.0609	1.69 ± 0.227	0.0465 ± 0.0449	11.9 ± 2.23	0.0522 ± 0.0130	0.842 ± 0.0701	354 ± 16.3
superior	r	1.40 ± 0.253	0.463 ± 0.0416	1.78 ± 0.237	0.0750 ± 0.0303	12.4 ± 2.29	0.0570 ± 0.0143	0.859 ± 0.0792	359 ± 17.3
	l	1.42 ± 0.245	0.457 ± 0.0433	1.78 ± 0.202	0.0772 ± 0.0331	12.3 ± 2.43	0.0567 ± 0.0140	0.858 ± 0.0737	360 ± 17.4

Table 3: Calculated model parameter and foveal characteristics grouped by gender and divided into main anatomical directions. The values in the table show the mean and the standard deviation over all subjects in the specified group. The rows of the table are split into three main groups which are (1) all, (2) male, and (3) female subjects. For each mentioned group, model parameters and foveal characteristics are given by a median value of the 40 fitted directions or by a value in one of the four anatomical directions (nasal, temporal, inferior, and superior). Furthermore, each row is divided into left and right eyes. For every entry in the table, the mean and the standard deviation is given. While the model parameters are unit-less, the used units for foveal slope, bowl area, radius, and rim height can be found in the table heading.

Acknowledgment

The authors would like to thank Peter K. Ahnelt, (retired from Div. of Neurophysiology und Neuropharmacology, Medical University Vienna, Austria) for helpful discussions regarding the histological material used for comparsion. We further gratefully acknowledge that Professor Ahnelt provided an additional light microscopy measurement of maximum rim height. Furthermore, we would like to thank Carolin Blankenburg, Marlen Kendziora (both Beuth University of Applied Science, Berlin, Germany) and Silvana Hermsdorf (Ernst Abbe University of Applied Sciences, Jena, Germany) for assistance with examining study subjects. Finally, the authors thank Ms Sylvina Eulitz, Leipzig University Hospital, Department of Opthalmology, Leipzig, Germany for her help with data management.

References

Ahnelt, P., . "Light microscopy measurement" personal communication, Div. of Neurophysiology und Neuropharmacology, Medical University Vienna, Austria.

Anger, E.M., Unterhuber, A., Hermann, B., Sattmann, H., Schubert, C., Morgan, J.E., Cowey, A., Ahnelt, P.K., Drexler, W., . Ultrahigh resolution optical coherence tomography of the monkey fovea. identification of retinal sublayers by correlation with semithin histology sections 78, 1117–1125.

Armstrong, R.A., . Statistical guidelines for the analysis of data obtained from one or both eyes 33, 7–14. doi:10.1111/opo.12009.

Benson, S., Schlottmann, P., Bunce, C., Charteris, D., . Comparison of macular hole size measured by optical coherence tomography, digital photography, and clinical examination 22, 87–90.

Chen, Y., Lan, W., Schaeffel, F., . Size of the foveal blue scotoma related to the shape of the foveal pit but not to macular pigment 106, 81–89. doi:dx.doi.org/10.1016/j.visres.2014.10.011.

Chui, T.Y.P., VanNasdale, D.A., Elsner, A.E., Burns, S.A., . The association between the foveal avascular zone and retinal thicknessfoveal avascular zone and retinal thickness 55, 6870. doi:10.1167/iovs.14-15446.

Delori, F.C., Goger, D.G., Keilhauer, C., Salvetti, P., Staurenghi, G., . Bimodal spatial distribution of macular pigment: evidence of a gender relationship 23, 521–538. doi:10.1364/JOSAA.23.000521.

Drexler, W., Fujimoto, J.G., . Optical coherence tomography: technology and applications. Springer Science & Business Media.

Dubis, A.M., Hansen, B.R., Cooper, R.F., Beringer, J., Dubra, A., Carroll, J., a. Relationship between the foveal avascular zone and foveal pit morphology 53, 1628–1636. doi:10.1167/iovs.11-8488.

Dubis, A.M., McAllister, J.T., Carroll, J., b. Reconstructing foveal pit morphology from optical coherence tomography imaging 93, 1223–1227. doi:10.1136/bjo.2008.150110.

Duker, J., Puliafito, C., Wilkins, J., Coker, J., Reichel, E., Hee, M., M., Fujimoto, J., . Imaging fellow eyes in patients diagnosed with idiopathic macular holes using optical coherence tomography (oct) 102, 118.

Early Treatment Diabetic Retinopathy Study Research Group, . Early photocoagulation for diabetic retinopathy: Etdrs report number 9 98, 766–785.

Fine, B., Yanoff, M., . Ocular histology: a text and atlas. Harper Collins Publishers.

Franco, E., Finlay, B., Silveira, L., Yamada, E., Crowley, J., . Conservation of absolute foveal area in new world monkeys 56, 276–286. doi:10.1159/000047211.

Garway-Heath, D.F., Rudnicka, A.R., Lowe, T., Foster, P.J., Fitzke, F.W., Hitchings, R.A., . Measurement of optic disc size: equivalence of methods to correct for ocular magnification 82, 643–649. doi:10.1136/bjo.82.6.643.

Grover, S., Murthy, R.K., Brar, V.S., Chalam, K.V., a. Comparison of retinal thickness in normal eyes using stratus and spectralis optical coherence tomography 51, 2644. doi:10.1167/iovs.09-4774, arXiv:/data/Journals/IOVS/933454/z7g00510002644.pdf.

Grover, S., Murthy, R.K., Brar, V.S., Chalam, K.V., b. Normative data for macular thickness by high-definition spectral-domain optical coherence tomography (spectralis) 148, 266–271. doi:10.1016/j.ajo.2009.03.006.

Heussen, F.M., Ouyang, Y., McDonnell, E.C., Narala, R., Ruiz-Garcia, H., Walsh, A.C., Sadda, S.R., . Comparison of manually corrected retinal thickness measurements from multiple spectral-domain optical coherence tomography instruments 96, 380–385. doi:10.1136/bjo.2010.201111.

Huang, D., Swanson, E., Lin, C., Schuman, J., Stinson, W., Chang, W., Hee, M., Flotte, T., Gregory, K., Puliafito, C., et, a., . Optical coherence tomography 254, 1178–1181. doi:10.1126/science.1957169.

Jonnal, R.S., Kocaoglu, O.P., Zawadzki, R.J., Lee, S.H., Werner, J.S., Miller, D.T., . The cellular origins of the outer retinal bands in optical coherence tomography imagescellular origins of the oct outer retinal bands 55, 7904–7918. doi:10.1167/iovs.14-14907.

Kang, S., Ahn, K., Ham, D., . Types of macular hole closure and their clinical implications 87, 1015–1019. doi:10.1136/bjo.87.8.1015.

Kirby, M.L., Galea, M., Loane, E., Stack, J., Beatty, S., Nolan, J.M., . Foveal anatomic associations with the secondary peak and the slope of the macular pigment spatial profile 50, 1383–1391. doi:10.1167/iovs.08-2494.

Krebs, I., Hagen, S., Smretschnig, E., Womastek, I., Brannath, W., Binder, S., a. Conversion of stratus optical coherence tomography (oct) retinal thickness to cirrus oct values in age-related macular degeneration 95, 1552–1554. doi:10.1136/bjo.2010.194670.

Krebs, I., Smretschnig, E., Moussa, S., Brannath, W., Womastek, I., Binder, S., b. Quality and reproducibility of retinal thickness measurements in two spectral-domain optical coherence tomography machines 52, 6925. doi:10.1167/iovs.10-6612.

Krebs, W., Krebs, E., . Primate retina and choroid 8, 134.

O'Leary, D.J., . The radius of curvature of the human foveal pit 68, 179–182. doi:10.1111/j.1444-0938.1985.tb00999.x.

Provis, J.M., Dubis, A.M., Maddess, T., Carroll, J., . Adaptation of the central retina for high acuity vision: Cones, the fovea and the avascular zone 35, 63–81. doi:10.1016/j.preteyeres.2013.01.005.

Reichenbach, A., Savvinov, A., Wurm, A., Grosche, J., Guck, J., Franze, K., Skatchkov, S.N., Agte, S., Junek, S., . Live cells as optical fibers in the vertebrate retina. INTECH Open Access Publisher.

Scheibe, P., Lazareva, A., Braumann, U.D., Reichenbach, A., Wiedemann, P., Francke, M., Rauscher, F.G., . Parametric model for the 3D reconstruction of individual fovea shape from {OCT} data 119, 19–26. doi:10.1016/j.exer.2013.11.008.

Shin, J., Chu, Y., Hong, Y., Kwon, O., Byeon, S., . Determination of macular hole size in relation to individual variabilities of fovea morphology .

Sigelman, J., Ozanics, V., . Ocular anatomy, embryology and teratology.

Tick, S., Rossant, F., Ghorbel, I., Gaudric, A., Sahel, J.A., Chaumet-Riffaud, P., Paques, M., . Foveal shape and structure in a normal population 52, 5105–5110.

Vajzovic, L., Hendrickson, A.E., O'Connell, R.V., Clark, L.A., Tran-Viet, D., Possin, D., Chiu, S.J., Farsiu, S., Toth, C.A., . Maturation of the human fovea: Correlation of spectral-domain optical coherence tomography findings with histology 154, 779–789.e2. doi:10.1016/j.ajo.2012.05.004.

Valentin, G., . Ein Beitrag zur Kenntniss der Brechungsverhältnisse der Thiergewebe 19, 78–105. doi:10.1007/BF01639843.

Wagner-Schuman, M., Dubis, A.M., Nordgren, R.N., Lei, Y., Odell, D., Chiao, H., Weh, E., Fischer, W., Sulai, Y., Dubra, A., et al., . Race- and sex-related differences in retinal thickness and foveal pit morphology 52, 625–634. doi:10.1167/iovs.10-5886.

Walls, G.L., . The vertebrate eye and its adaptive radiation. Bloomfield Hills, Michigan, Cranbrook Institute of Science.

Wolf-Schnurrbusch, U.E.K., Ceklic, L., Brinkmann, C.K., Iliev, M.E., Frey, M., Rothenbuehler, S.P., Enzmann, V., Wolf, S., . Macular thickness measurements in healthy eyes using six different optical coherence tomography instruments 50, 3432. doi:10.1167/iovs.08-2970.

Wolfram Research, I., . Mathematica. Wolfram Research, Inc. URL: http://www.wolfram.com/mathematica. version 10.3.

Yanni, S.E., Wang, J., Chan, M., Carroll, J., Farsiu, S., Leffler, J.N., Spencer, R., Birch, E.E., . Foveal avascular zone and foveal pit formation after preterm birth 96, 961–966. doi:10.1136/bjophthalmol-2012-301612.

Yuodelis, C., Hendrickson, A., . A qualitative and quantitative analysis of the human fovea during development 26, 847–855. doi:10.1016/0042-6989(86)90143-4.

Zocher, M.T., Rozema, J.J., Oertel, N., Dawczynski, J., Wiedemann, P., Rauscher, F.G., . Biometry and visual function of a healthy cohort in leipzig, Germany .